JGR Space Physics

Key Points:

- Estimated detection altitudes of ionospheric perturbations in Global Positioning System (GPS)-Total Electron Content (TEC) as induced by the Rayleigh wave following the Tohoku-Oki earthquake
- Possible detection of specific ionospheric perturbations progressively at different altitudes based on varying satellite geometries
- Rayleigh wave sources for the generation of the subsequent ionospheric perturbations have been identified by using seismic waveform data

Supporting Information:

Supporting Information may be found in the online version of this article.

Correspondence to:

M. S. Bagiya,
bagiyamala@gmail.com;
mala.bagiya@iigm.res.in

On the Rayleigh Wave Induced Ionospheric Perturbations During the Mw 9.0 11 March 2011 Tohoku-Oki Earthquake

Dhanya Thomas[1,2], Mala S. Bagiya[1] ⓘ, Nava Kumar Hazarika[3], and D. S. Ramesh[1]

[1]Indian Institute of Geomagnetism, Navi Mumbai, India, [2]CSIR Fourth Paradigm Institute (CSIR-4PI), Bangalore, India, [3]Shillong Geophysical Research Center, Indian Institute of Geomagnetism, Shillong, India

Abstract Spatial and temporal characteristics of Rayleigh wave generated ionospheric perturbations are well documented based on the ionospheric measurements using Global Positioning System (GPS)-Total Electron Content (TEC) technique. However, due to integrated nature of the GPS recorded TEC, the actual detection altitudes of these perturbations could not be determined. In general, the maximum electron density altitude (hmF2) is assumed as the perturbation detection altitude in GPS-TEC. To validate this assumption, case studies focusing on the early detection of ionospheric perturbations induced by direct epicentral waves during the Mw 7.4 9 March 2011 Sanriku-Oki and Mw 9.0 11 March 2011 Tohoku-Oki earthquakes were performed. In the present study, we attempt to estimate the detection altitudes of GPS-TEC derived ionospheric perturbations generated by the propagating Rayleigh surface waves following the Mw 9.0 11 March 2011 Tohoku-Oki earthquake. Based on the 3D ray tracing of Rayleigh wave generated acoustic waves in the atmosphere and realistic GPS station-satellite line of sight geometry, we could efficaciously compute the actual detection altitudes of Rayleigh wave generated coseismic ionospheric perturbations (CIPs). Further, our study also demonstrates the possible detection of CIPs progressively at different altitudes based on varying satellite geometries.

1. Introduction

The piston effect of the crustal deformation near the earthquake source region and the displacement associated with the propagating Rayleigh surface waves can generate atmospheric wave perturbations. These waves propagate upward with increasing amplitudes to conserve the energy in a medium of decreasing neutral density. When these wave perturbations reach at the ionospheric altitudes, they can redistribute the ionospheric plasma through ion-neutral collision and generate the electron density perturbations. These coseismic ionospheric perturbations (CIPs) are detected using various observational techniques such as Doppler sounding, ionosonde, over the horizon (OTH) radar, air glow imagers, radio occultation and Global Navigation Satellite System (GNSS), etc. (Artru et al., 2004; Bagiya et al., 2017; Coisson et al., 2015; Heki & Ping, 2005; Makela et al., 2011; Maruyama et al., 2017; Occhipinti et al., 2010; Sunil et al., 2015). With the deployment of dense GNSS receiver network in various parts of the globe, the studies related to earthquake generated ionospheric perturbations became more frequent.

There are mainly three types of atmospheric wave perturbations which can be observed during earthquakes. The acoustic waves generated due to the sudden vertical displacement of the Earth's crust, Rayleigh wave generated acoustic waves and tsunami generated gravity waves (if earthquake occurs offshore). In general, the CIP observed within ~500–800 km of epicenter are considered to be generated by the direct epicentral waves (Bagiya et al., 2017; Otsuka et al., 2006; Sunil et al., 2017). This radial distance apparently depends on the dimension of the fault plane. In addition to this, the propagating Rayleigh surface waves can also produce ionospheric perturbations away from the epicenter. Thus, the CIPs generated by direct epicentral waves are generally captioned as the near-field CIPs while those by Rayleigh surface waves are termed as the far-field. It is to be noted that earthquakeinduced ionospheric perturbations were first reported after the detection of Rayleigh wave generated CIP during the 1964 Alaska earthquake (Davies & Baker, 1965; Leonard & Barnes, 1965). The CIP of Rayleigh wave origin has been observed and studied using various ionospheric probing techniques since then (Ducic et al., 2003; Liu & Jin, 2019; Maruyama et al., 2017; Rolland et al., 2011; Weaver et al., 1970; Yuen et al., 1969).

The Global Positioning System (GPS)-Total Electron Content (TEC) technique is extensively used to study the earthquake-induced ionospheric perturbations, owing to its global coverage and continuous availability (Artru

et al., 2005; Astafyeva & Shults, 2019; Bagiya et al., 2017; Calais & Minster, 1995; Ducic et al., 2003; Heki & Ping, 2005; Jin et al., 2015; Komjathy et al., 2016; Liu et al., 2006; Occhipinti et al., 2013; Rolland et al., 2011; Sunil et al., 2017). The first detection of Rayleigh wave induced CIP using GPS-TEC was documented after the Denali Alaska earthquake in 2002 (Ducic et al., 2003). Subsequently, the Rayleigh wave generated ionospheric perturbations have been studied extensively by using GPS-TEC technique (Artru et al., 2004; Astafyeva et al., 2009; Ducic et al., 2003; Jin et al., 2014; Liu et al., 2011; Occhipinti et al., 2010, 2018; Rolland et al., 2011). The GEONET (GPS Earth Observation Network System), Japan, with more than 1,200 GPS stations, was used to study the amplitude evolution, propagation pattern, direction, and velocity of the Rayleigh wave generated CIP during the Tohoku-Oki event (e.g., Jin et al., 2014; Liu et al., 2011,2016). Thus, the GPS-TEC technique can provide reasonable measure of the spatio-temporal evolutions of Rayleigh surface wave generated ionospheric perturbations. However, due to the integrated nature of GPS-TEC, the detection altitudes of these perturbations could not be determined earlier. Generally, the detection altitude of the ionospheric disturbances recorded in the GPS-TEC is assumed to be at the maximum electron density altitude/hmF2. However, this assumption is not always true. By assuming the detection altitude of the ionospheric disturbance at the maximum electron density altitude in GPS-TEC, Ozeki and Heki (2010) and Kakinami et al. (2013) attempted to estimate the exact trajectories of the missile launches at ionospheric altitudes. However, they found that the exact trajectories of the missile will only coincide if the detection of the perturbation occur at different altitudes other than the maximum electron density altitude. Further, Astafyeva et al. (2011, 2013) studied the early arrivals of CIPs observed during Mw 9.0 Tohoku-Oki earthquake to retrieve the seismic source parameter from its ionospheric signature. They suggested that the position of the ionospherically detected seismic source and seismologically modeled ground source will have a better agreement when lowering the detection altitude from the maximum electron density altitude. Later, Thomas et al. (2018) examined the validation of the assumption of maximum electron density altitude as the perturbation detection altitudes in GPS-TEC by studying the early arrivals of CIPs observed in GPS-TEC during the Mw 7.4 Sanriku-Oki earthquake. Using a simple ray tracing approach, they not only estimated the exact detection altitude of the CIP recorded in the GPS-TEC but also explained the reason for the observed early arrivals of CIPs. They found that the early arrival of CIPs is due to the detection of CIPs at lower ionospheric altitudes instead of hmF2. Furthermore, by applying the proposed method of Thomas et al. (2018) to the Mw 9.0 Tohoku-Oki earthquake, Bagiya et al. (2020) could estimate the detection altitude of GPS-TEC derived coseismic ionospheric signatures and also delineated the distinct ground seismic sources responsible for the generation of these perturbations, which evolved during the initial 60 s of the Tohoku rupture. Moreover, they could derive reasonably the precise reflection of the seismic rupture extent in the ionosphere. Recently, Kakinami et al. (2013) studied the onset altitude of the CIPs during the Mw 7.4 Sanriku-Oki earthquake and they found that the geographic coordinates of the onset point will only coincide if the CIPs are assumed at different altitudes. Shifting the detection altitude of the onset point to different ionospheric altitudes they could estimate the vertical velocity of the acoustic-gravity wave and source location using the GPS-TEC data.

Moreover, the horizontal propagation velocity of the CIPs is estimated by considering the coseismic ionospheric disturbances at fixed height of maximum electron density. The propagation velocity estimation can be erroneous as the actual detection height of coseismic ionospheric disturbances can vary over the ionospheric height range of ~120–~250 km (Bagiya et al., 2020; Thomas et al., 2018). Also, sounding the rupture area and retrieving the source information using its ionospheric signatures has always been the topic of interest. The detection altitude along with elevation angle determines the location of the Ionospheric Piercing Point (IPP). Thus, changing the detection altitude will change the IPP location (Astafyeva et al., 2013) and which results into the change in seismic source location while retrieving it from the ionospheric signatures. This shows the importance of studying the actual detection altitude of the coseismic ionospheric disturbances in GPS-TEC by focusing on various source characteristics. So far, the detection altitude of the CIPs induced by the direct epicentral waves could study in detail to a certian extent. However, there is no studies has been carried out to explore the detection altitude of the Rayleigh wave induced CIPs. In this paper, we study in detail the detection altitude of the Rayleigh wave induced CIPs during Mw 9.0 11 March 2011 Tohoku-Oki earthquake. Further, based on the distinct GPS satellite geometries the detection of specific CIP at various ionospheric altitudes is also demonstrated.
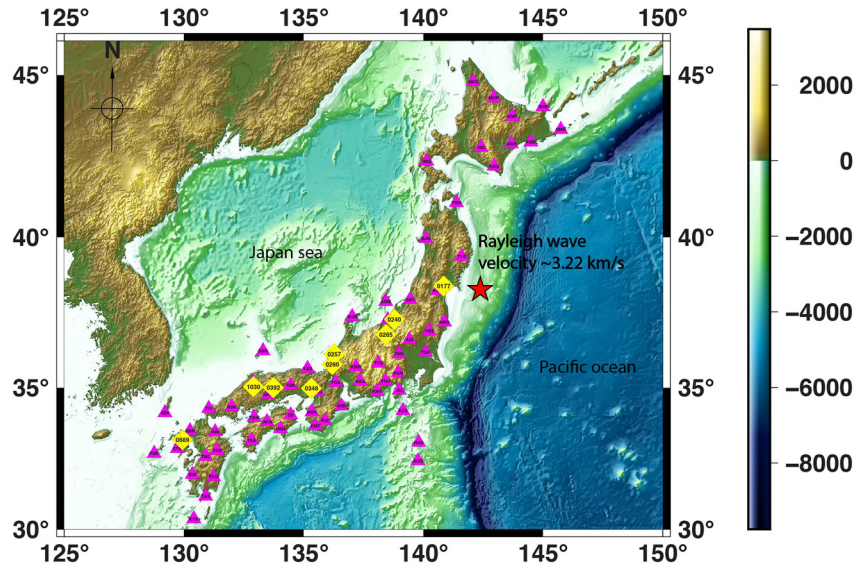
Figure 1. Map showing the locations of nine Global Positioning System (GPS) stations and 62 seismic stations used in the study. Yellow diamonds are the location of GPS station and magenta triangles are the seismometer locations. Each triangle and diamonds are labeled with the corresponding station name. The red star shows the epicenter.

2. Data and Methodology

2.1. GPS-TEC Derived CIP

The main parameter that requires to estimate the CIP detection altitude is the onset time of the recorded ionospheric perturbations in GPS-TEC (Thomas et al., 2018). To estimate the onset time of the Rayleigh wave induced CIP with maximum accuracy, the high rate 1s GEONET data over the Japan Island were analyzed. The CIP has been identified based on the discernible TEC fluctuations as observed in slant TEC (sTEC) time series. The onset time of CIP is the time when the sTEC starts to suddenly increase or decrease with respect to its background TEC value. This onset time is determined manually by following Astafyeva et al. (2011).

In the present study, the sTEC has been estimated using the carrier phase measurements of GPS signals using the following equation:

$$\text{sTEC}_{\text{code}} = \frac{1}{40.3}\left(\frac{f_1^2 f_2^2}{f_1^2 - f_2^2}\right)(L_1\lambda_1 - L_2\lambda_2) \tag{1}$$

where f_1 and f_2 are the carrier frequencies (f_1 = 1575.42 MHz, f_2 = 1227.60 MHz). λ_1 and λ_2 are the corresponding wavelengths, and L_1 and L_2 are the carrier phases at f_1 and f_2 frequencies. Further, we compute the GPS satellite line of sight (LOS) using the satellite navigation data and receiver coordinates. The receiver coordinates are derived using the precise point positioning mode (Zumberge et al., 1997).

2.2. Rayleigh Wave Propagation in Seismometer Data

The ground seismic sources are considered in terms of the propagating Rayleigh surface waves. To start with, the Rayleigh surface wave velocity over the Japan region has been estimated based on the seismic waveform data recorded during the Tohoku-Oki earthquake (http://www.fnet.bosai.go.jp). The locations of 62 seismometers used in the present study are shown in Figure 1 in magenta triangles. The waveform data from these seismic stations were analyzed using the SEISAN seismic software (Havskov & Ottemöller, 1999). Thereafter, the arrival time of Rayleigh wave at each seismometer location has been carefully estimated using the vertical seismic wave component.

The vertical component of the seismic wave with increasing epicentral distance from the 62 seismic stations is stacked and presented in Figure S1 in Supporting Information S1. A linear increase in the arrival time with the

epicentral distance can be seen in the figure. To estimate the average Rayleigh wave velocity over the Japan, a travel time diagram is prepared (Figure S2 in Supporting Information S1). Based on the slope of the best fitted line, the average Rayleigh wave velocity over the Japan region during the Tohoku-Oki main shock has been estimated as ∼3.22 km/s. The postfit residuals are also shown in Figure S2 in Supporting Information S1. It is worth to note that the obtained velocity is well corroborated with the earlier reported Rayleigh surface wave velocity over the Japan (e.g., Takagi et al., 2006; Witek et al., 2014).

2.3. Determining the Locations of Ground Seismic Sources

We use 1s GPS data and thus the minimum resolvable temporal scale while estimating the CIP onset time is 1 s. Rayleigh surface wave with an average ground velocity of 3.22 km/s may travel ∼3.22 km distance within 1 s. Thus, the spatial resolution of seismic sources can be visualized as 3.22 km in the present case. Based on this, we assume the ground Rayleigh wave sources at every 3.22 km of spatial interval.

2.4. 3D Ray Tracing of Rayleigh Wave Induced Acoustic Waves in the Atmosphere

The ray tracing of the Rayleigh wave generated acoustic waves differ from the ray tracing of the acoustic waves generated by the sudden vertical displacement near the epicenter. The propagation of Rayleigh wave generated seismo-acoustic rays is not hemispherical, instead they propagate in a conical shape (Najita & Yuen, 1979; Rolland et al., 2011). The speed of the propagating Rayleigh wave at ground (∼3.22 km/s) is higher as compared to the speed of the sound in the atmosphere (0.337 km/s). This velocity difference determines the initial thrust angle/launching angle with which the generated acoustic waves propagate upward in the atmosphere. Also, the upward propagating seismo-acoustic waves lag behind the fast propagating ground seismic source and hence, the Rayleigh wave-induced acoustic wave front propagates in a conical shape. The conical shaped acoustic wave front and Rayleigh wave induced acoustic wave traces are illustrated in the schematic of Figure 2a. The geometry to estimate the launching angle/initial thrust angle θ of generated acoustic waves is also shown in the figure. The launching angle is estimated by using Equation 2. It could be noticed that angle computation is linked to the initial velocity of atmospheric acoustic wave and velocity of Rayleigh wave at the ground. The average velocity of acoustic wave (∼0.337 km/s) near the surface is estimated based on the NRLMSISE-00 model. Using Equation 2, the initial thrust/launching angle is computed as 5.97° during this event

$$\tan(\theta) = \frac{\text{Acoustic wave velocity near the surface}}{\text{Rayleigh wave velocity at ground}} \tag{2}$$

The assumed Rayleigh wave sources at every 3.22 km of distance, away from the epicenter, can generate subsequent acoustic waves in the atmosphere. These acoustic waves propagate upward and undergo refraction in the medium of varying temperature and density. To trace the propagation of Rayleigh wave induced acoustic waves, the acoustic wave velocity has been estimated at every 1 km of atmospheric altitude by using Equation 3.

$$V = \sqrt{\frac{\gamma R T}{M}} \tag{3}$$

Here, γ is the specific heat capacity, R is the universal gas constant, T is the temperature, and M is the molecular mass density.

By using the ray tracing procedure, the arrival times and traces of Rayleigh wave induced acoustic waves at different atmospheric altitudes are computed. The Rayleigh waves after any earthquake propagate outward over a wide azimuthal direction (0°–360°) from the epicenter. Therefore, the seismic sources are considered at every 1° of azimuthal interval and at every 3.22 km of distance around the epicenter. It should be noted that initial propagation time of the induced acoustic waves largely depends on the manifestations of Rayleigh wave seismic sources. In other words, the acoustic waves that are generated at every 3.22 km distance is delayed by ∼1 s as that of the earlier source. This delay has been accounted for while computing the seismo-acoustic ray traces. The atmospheric propagation of Rayleigh wave induced acoustic waves for the sources considered at every 3.22 km, starting from epicenter up to ∼1,000 km of distance, for all azimuthal direction has been modeled. The 3D model output of ray traces up to ∼100 km distance from the epicenter can be seen in Figure 2b. For better representation,
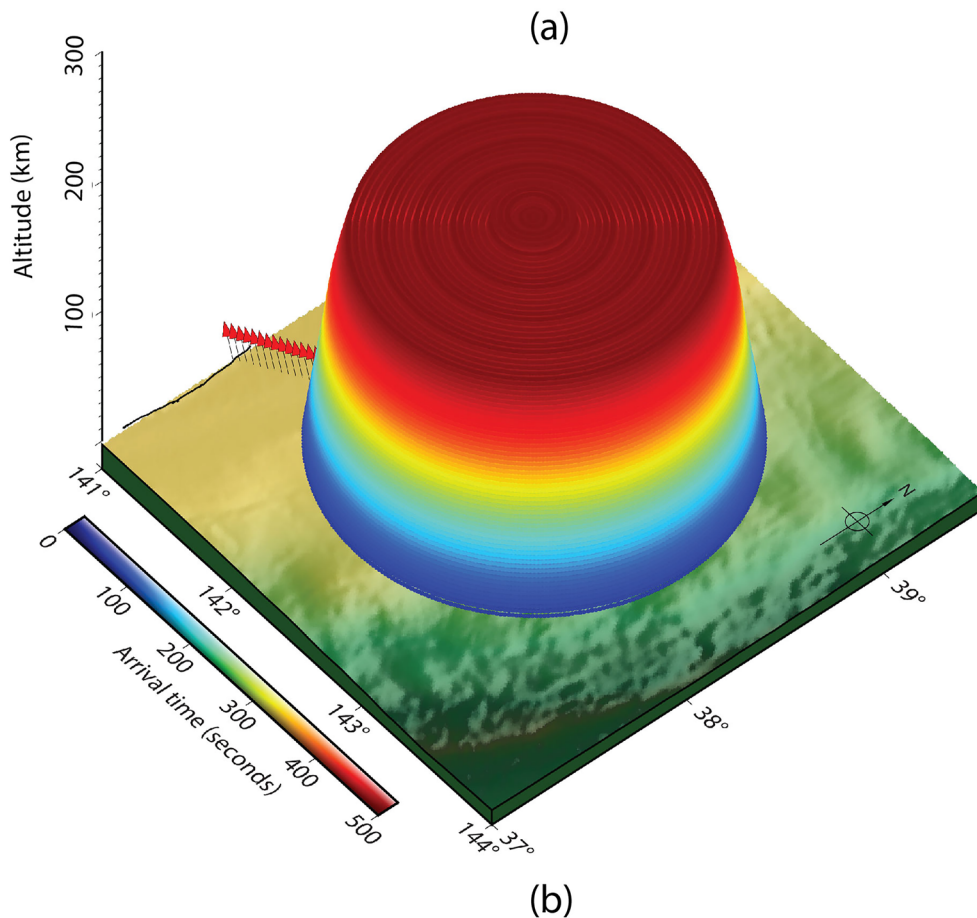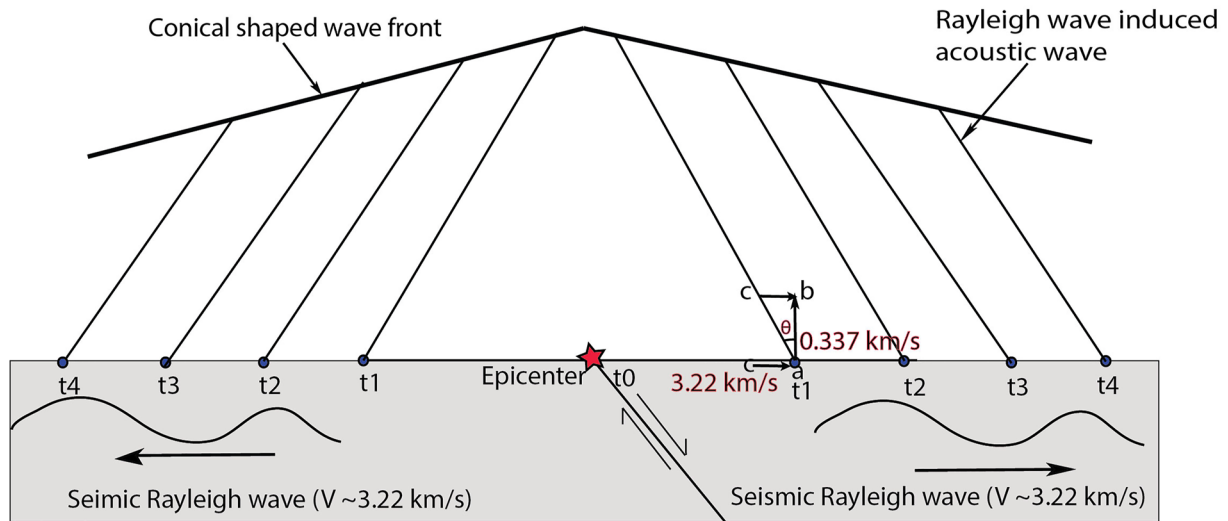
Figure 2. (a) Schematic showing atmospheric propagation of Rayleigh wave generated acoustic waves. The small blue disks correspond to the assumed seismic sources at every 3.22 km of distance. The vertically propagating acoustic waves along with the conical shaped wave front are shown. A simple geometry that allows to estimate the initial thrust angle is also shown. (b) Modeled spatial and temporal propagation of Rayleigh wave induced acoustic rays by considering the seismic sources at every 3.22 km of distance and 1° of azimuthal interval from the epicenter. The red headed arrow shows the location of Rayleigh wave sources.

the rays are restricted to evolve till 630 s in the figure. It could be noticed that the rays are propagating conical in shape all around the epicenter and almost vertical from the respective source region.

3. Estimation of the Detection Altitudes of Rayleigh Wave Generated CIPs Based on GPS-TEC Measurements

First, in order to differentiate the CIP generated by Rayleigh wave sources from that of the near-field CIP, the following criteria has been adopted. From Figure 2a of Bagiya et al. (2020), the seismic energy mostly propagated east of the epicenter during the initial 60 s of rupture. Also, it is understood that the seismo-acoustic rays propagating upward from the source location reach almost near horizontal up to 200 km at IPP altitude (the intersecting point of satellite LOS with the assumed thin ionospheric shell, here it is 250 km) within 700 s from the event onset time. This is based on the ray tracing analysis for direct epicentral waves during the Tohoku-Oki event as reported in Bagiya et al. (2020). However, the Rayleigh wave generated ionospheric perturbations can be observed far-field, i.e., away from the epicenter. Astafyeva et al. (2009) reported that Rayleigh wave generated ionospheric perturbations are not distinguishable until further than 600–700 km away from the epicenter. Liu and Jin (2019) reported Rayleigh wave induced ionospheric perturbations starting from 200 km of the epicenter during Alaska 2018 event. Tsugawa et al. (2011) reported that Rayleigh wave induced perturbations were the first to get detected in the ionosphere and not those induced by direct epicentral waves during Tohoku-Oki event.

In the present analysis, we consider arrival of Rayleigh waves at three different locations from the epicenter. These are at 350, 650, and 950 km. The considered Rayleigh wave arrivals can be at any azimuth angle. The Rayleigh waves arriving at these distances are named as RW350, RW650, and RW950, respectively. The propagating Rayleigh wave can generate acoustic waves in the atmosphere. Accordingly, RW350, RW650, and RW950 are considered as acoustic wave sources. The selection of the sources is arbitrary and any change in the source location will not alter the outcome of present analysis. To examine the ionospheric variations generated by RW350 source, we selected station 0240 which is located near this source. The CIP recorded by PRN27 from GPS station 0240 is first considered here. The GPS satellite PRN27 was orbiting with an elevation angle of ~80°–90°.

Figure 3a shows the sTEC time series recorded by PRN27 from station 0240. The elevation angle at the time of CIP onset is shown in magenta and the observed CIP onset time is highlighted using a red dot. In Figure 3b, the observed onset time is displayed at the corresponding IPP location (the colored disk highlighted in magenta circle). The IPP altitude is estimated as 250 km by estimating the maximum electron density altitude based on the electron density distribution as a function of altitude taken from the IRI 2016 model (Bilitza et al., 2017). The horizontal cross section of the modeled arrival times at IPP altitude is presented as the colored background in the figure. It should be noted that the recorded onset time (671 s) is earlier than the modeled time (726 s) (please see the background color and colored disk), which implies the possibility of CIP detection at lower altitudes (early detection) similar to the reported cases of Sanriku-Oki Tohoku foreshock and Tohoku-Oki main shock.

To estimate the detection altitude of Rayleigh wave generated CIP, the intersection of the satellite LOS with that of the ray arrival at each instant of time has been examined by following the method of Thomas et al. (2018). First, we model the seismo-acoustic rays induced by the propagating Rayleigh wave by considering the ground source at every 3.22 km starting from the epicenter. Further, we determine the first intersecting point between satellite LOS and the modeled ray traces as a function of altitude within the observed CIP onset time. Whenever the satellite LOS intersects with acoustic ray, it can detect CIP generated by that ray. Here, the intersection is preferred to occur within the observed CIP onset time and the intersection altitude has been estimated as the CIP detection altitude. When satellite LOS intersects with the propagating seismo-acoustic ray, we extract the modeled time and compare it with the observed onset time for any residual error. The intersections of PRN27 satellite LOS from station 0240 to seismo-acoustic rays have been examined for the rays modeled for RW350 and nearby sources. This computation has been repeated till the minimum residual error between the observed onset time of CIP and the modeled time is obtained. It should be noted that minimum residual error for the intersection between PRN27 LOS and modeled acoustic rays occurred when the source is at 383.18 km. Therefore, CIP detected by PRN27 from station 0240 was perhaps generated by Rayleigh wave source located at 383.18 km. Figure 3c shows the spatial and temporal evolution of acoustic waves generated by the RW383.18 source. It also contains the interaction of PRN27 LOS from 0240 station to modeled acoustic rays. The analysis suggests that LOS and seismo-acoustic rays started to intersect at an altitude of 207 km within 664 s. It could be seen that intersection
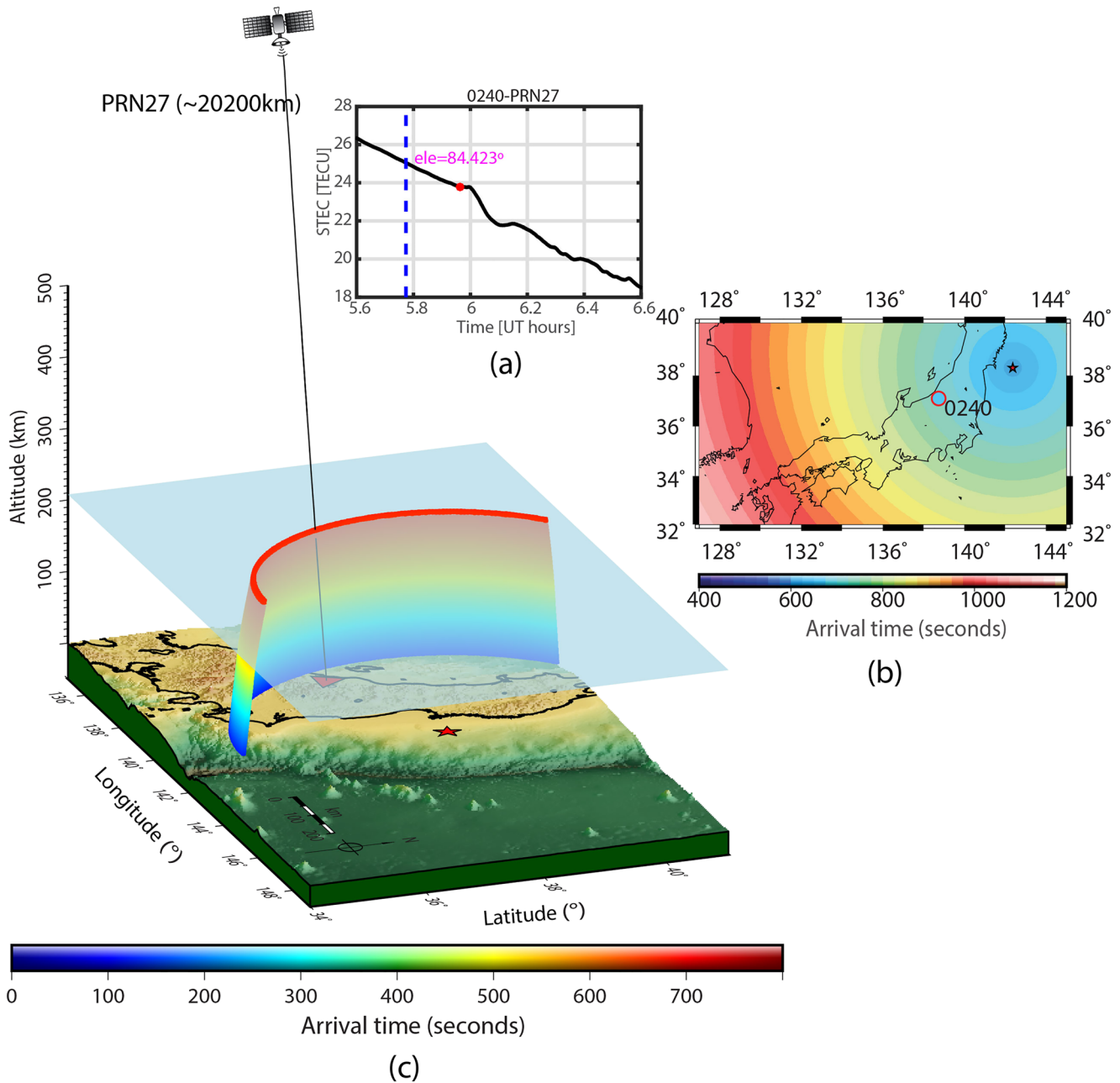
Figure 3. (a) Global Positioning System (GPS)-Total Electron Content (TEC) time series corresponding to PRN27 for station 0240. The blue dashed line is plotted at the earthquake onset time. Red dot in the time series represents the observed onset time of Coseismic Ionospheric Perturbation (CIP). Corresponding elevation angle is given in magenta. (b) Background color is the modeled arrival time of acoustic waves and red outlined disk shows the observed onset time of CIP from 0240 GPS station. The disk is placed at the Ionospheric Piercing Point (IPP) altitude of 250 km. (c) Intersection of GPS satellite line of sight (LOS) with modeled seismo-acoustic ray traces for station 0240 is shown. LOS of PRN27 is plotted at the observed onset time of CIP. The location of the station is shown in red triangle. The 3D acoustic ray traces are shown for azimuthal angles ranging from ~0° to 140°. The altitude of first intersection of LOS with the rays is highlighted using a transparent plane.

did not occur at the observed onset time instead, the LOS started to intersect with the seismo-acoustic rays 8 s before the observed onset time. The altitude of intersection (207 km) is highlighted with a transparent plane in Figure 3c. It should be noted that estimated detection altitude is lower than the IPP height of 250 km. Thus, it is assumed that PRN27 LOS started to detect the CIP at lower ionospheric altitude (207 km). This significant finding could be appreciated in terms of computing, for the first time, the detection altitude of CIP measured in GPS-TEC and generated by propagating Rayleigh waves.

Table 1
3D Model Output Demonstrating the Estimation of Actual Detection Altitudes of Rayleigh Wave Generated Coseismic Ionospheric Perturbations (CIPs)

Station	PRN	Onset time (s)	Modeled time (s)	Elevation (°)	Seismic source (RW distance from epicenter (km))	Estimated detection altitude (km)	Difference between observed onset time and modeled time (s)
0240	27	672	664	84.42	RW383.18	207	8
0177	21	638	634	38.56	RW386.4	186	4
0260	26	631	630	33.31	RW386.4	183	1
0257	27	750	750	86.25	RW637.56	212	0
0265	21	733	731	40.85	RW640.78	198	1
0392	26	672	669	30.65	RW634.34	159	3
1030	27	903	898	84.16	RW969.22	245	5
0348	21	842	839	43.92	RW972.44	202	3
0689	26	803	800	25.87	RW969.22	176	3

Note. The station-PRN geometry, onset time, modeled time at the intersection between acoustic rays and satellite line of sight (LOS), elevation angle, corresponding seismic source, estimated detection altitude, and difference between observed onset time and modeled time are given.

The computation has been repeated for RW650 and RW950 sources. In case of RW650 source, the station-satellite combination of 0257-PRN27 was selected. Our analysis estimated the CIP detection altitude as 212 km. The modeled time at the intersection between satellite LOS and ray arrival is determined as 750 s (Table 1), which is well corroborated with the observed onset time (750 s). Further, our analysis suggests that RW637.56 source generated the CIP detected by PRN27 from 0257 station. In the case of distant Rayleigh wave source RW950, station-satellite combination of 1030-PRN27 was selected. The observed CIP onset time was 903 s. The modeled ray arrival time at the time of intersection was 898 s and the detection altitude is estimated as 245 km. The Rayleigh wave source that could generate the observed CIP has been identified as RW969.22 (Table 1). The discrepancy between the modeled time and observed onset time for 1030-PRN27 combination is 5 s.

The discrepancies observed between the modeled time and observed CIP onset time might be due to the assumed seismic source distribution at 3.22 km in addition to model-derived atmospheric parameters for acoustic ray tracing. As the propagation of Rayleigh wave at the ground generate almost vertical acoustic wave propagation in the atmosphere, the effect of wind is negligible (Lognonne et al., 2016; Rolland et al., 2011). In the present study, we have considered ground sources at every 3.22 km of distance based on the average Rayleigh wave velocity computed in Figure 1. Further, as mentioned in Thomas et al. (2018), the model-derived temperature and density parameters, which are used to estimate the acoustic wave velocity in the atmosphere, can also introduce error in estimation of CIP detection altitude. The aforementioned parameters may lead to the residual time errors.

4. Detection of CIP at Different Ionospheric Altitudes Using Various Satellite Geometries

The previous studies by Thomas et al. (2018) and Bagiya et al. (2020) have already demonstrated that detection of GPS-TEC-derived CIP cannot be considered at fixed height of maximum ionospheric electron density. These studies were carried out for the CIPs generated by direct epicentral waves. However, in this paper, we consider ionospheric perturbations generated by propagating Rayleigh surface waves and compute their actual detection altitudes. Further, we expand our approach to estimate the detection of CIP at different ionospheric altitudes based on suitable station-satellite geometries.

We consider the Rayleigh wave source of RW383.18 for this analysis. It has been demonstrated in earlier section that RW383.18 served as the generative source of CIP detected by station-satellite geometry of 0240-PRN27. To estimate the detection of this CIP at other altitudes, we need to search for the suitable station-satellite geometries. The intersection of various satellite LOS to the modeled acoustic rays generated by RW383.18 and nearby sources has been examined. After numerous iterations, 0177-PRN21 geometry is determined to detect the CIP
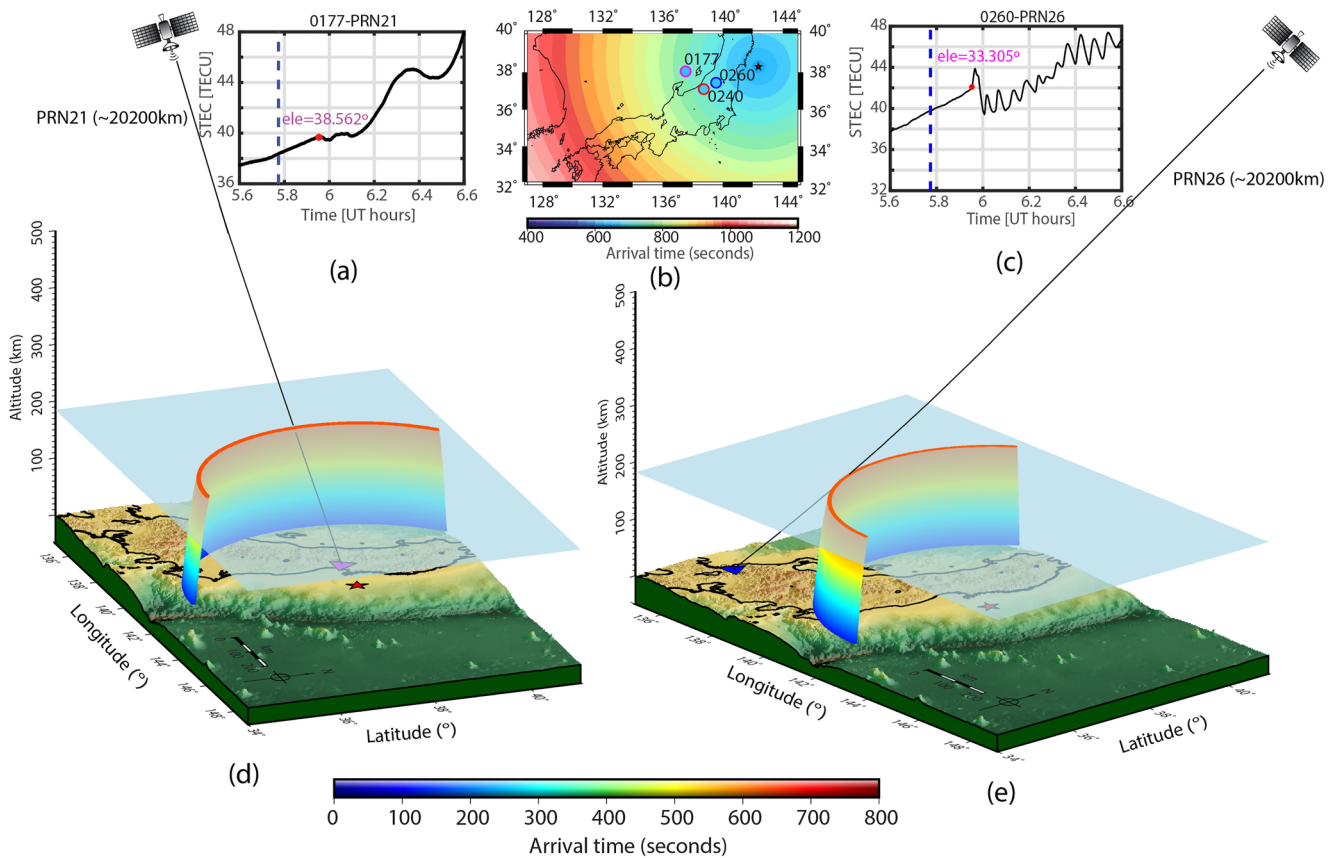
Figure 4. (a) Global Positioning System (GPS)-Total Electron Content (TEC) time series corresponding to PRN21 for station 0177. Other details are similar to Figure 3a. (b) Background color is the modeled arrival time of acoustic rays at Ionospheric Piercing Point (IPP) altitude and the colored disks are the observed Coseismic Ionospheric Perturbation (CIP) onset times as recorded by PRN27, PRN21, and PRN26. (c) Same as (a) but for the station-satellite 0260-PRN26 geometry. (d) Intersection of PRN21 line of sight (LOS) to acoustic rays for station 0177. LOS of PRN21 is plotted at the observed onset time of CIP. The station location is shown in magenta triangle. 3D acoustic ray traces are shown for azimuthal angles ranging from ~0° to 140°. The altitude of first intersection of LOS to the rays is highlighted using a transparent plane. (e) Same as (d) but for 0260-PRN26 geometry. The station location is shown in blue triangle.

generated by the source nearest to RW383.18. Our analysis suggests that Rayleigh wave source of RW386.4 could generate the CIP recorded by 0177-PRN21 combination. This source is 3.22 km away from that of the RW383.18. Figure 4a shows TEC time series recorded by 0177-PRN21. The observed detection time of CIP in PRN21 from station 0177 is shown in Figure 4b along with the CIP detection time in PRN27 from station 0240. The background color shows the modeled arrival time of acoustic rays at IPP altitude. Figure 4d shows the intersection of LOS with the modeled acoustic rays for 0177-PRN21 geometry. The first intersection between the satellite LOS and acoustic rays occurred at 634 s at an altitude of 186 km. The observed onset time of CIP from 0177-PRN21 was 638 s. The residual time difference is 4 s. It should be noted that estimated CIP detection altitude (186 km) is much lower than the IPP altitude (250 km) and also lower than the altitude estimated for the 0240-PRN27 geometry (207 km). The elevation angle of PRN21 at the CIP detection time was 38.56°. This shows another early CIP detection using the low elevation satellite geometry in addition to the observations reported during the Sanriku-Oki Tohoku foreshock and Tohoku-Oki main shock (Bagiya et al., 2020; Thomas et al., 2018). The reason for the low altitude detection of CIPs using low elevation geometry has explained in detail by Thomas et al. (2018) and Bagiya et al. (2020). They found that the lower elevation angle satellites which could sound directly above the source area starts to intersect with the CIPs from the very low ionospheric altitudes itself. In addition, the factors such as the station location, azimuth angle between source and satellite LOS are also plays a major role. Further, it is already well understood that the low elevation angle satellites are more efficient in detecting the CIPs in GPS-TEC that are generated by the ground Rayleigh waves (Rolland et al., 2011). In the search of further station-satellite geometries, our iterative analysis converged on 0260-PRN26 geometry which intersected with the acoustic rays from RW386.4. Here, the satellite LOS is intersected with the
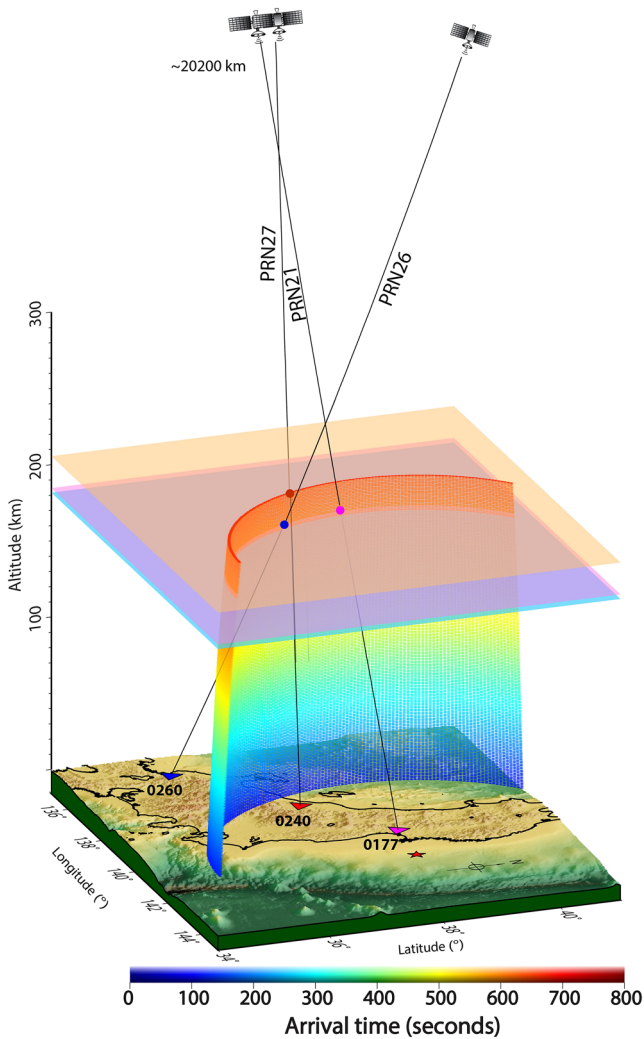
Figure 5. Coseismic Ionospheric Perturbation (CIP) detection at different ionospheric altitudes. Modeled acoustic ray traces and three satellite line of sight (LOS) geometries from three Global Positioning System (GPS) stations are shown. The stations are shown in triangle. The altitudes where LOSs intersected with the vertically propagating acoustic waves are highlighted with transparent planes. The planes and interaction points are also shown in the same color as that of the corresponding stations.

modeled ray at an altitude of 183 km at 630 s. The observed onset time of CIP for 0260-PRN26 geometry was 631 s. The temporal variations of CIP as recorded by 0260-PRN26 geometry are shown in Figure 4c. The detection time of this CIP is projected at IPP altitude in Figure 4b. Figure 4e shows the intersection of PRN26 LOS from 0260 station with the propagating acoustic waves generated by RW386.4 source. The elevation angle at the time of CIP detection was 33.30°. The low elevation angle facilitated the detection of CIP at lower ionospheric altitude than the IPP altitude.

Though dense GEONET GPS data have been used in the present analysis, we did not find any station-satellite geometry, other than 0240-PRN27, that could exactly sound the source RW383.18. After introducing a small shift in the source location and performing a large number of iterations, 0177-PRN21 and 0260-PRN26 combinations have been found suitable to sound the source region within 3.22 km (i.e., location of RW383.18 ± 3.22 km). The propagation velocity of Rayleigh surface wave has been estimated as 3.22 km/s. Thus, the maximum temporal error between the considered seismic sources, distributed at 3.22 km of distance, is ±1 s. Thereby, the acoustic wave generated by the source RW383.18 propagates with temporal difference of 1 s with respect to the acoustic wave generated by the nearby source. The maximum acoustic wave velocity in the atmosphere can be 1 km/s. The difference between the estimated detection altitudes of CIP (207, 186, and 183 km) for three different station-satellite geometries was higher than 1 km. Thus, the small shift introduced in the source location (∼3.22 km) is tolerable. It could be stated that the cautious selection of three different station-satellite geometries could capture the CIP, generated by Rayleigh waves, at different ionospheric altitudes during Tohoku-Oki event. These three station-satellite geometries are presented in Figure 5. The estimated detection altitudes are highlighted with three different transparent planes. Thus, in addition to the estimation of CIP detection altitudes, present analysis enabled the possible detection of specific CIP progressively at different ionospheric altitudes.

Further, we extended our analysis to find the suitable observation geometries which could detect ionospheric perturbations at different altitudes in cases of RW637.56 and RW969.22 sources. The number of iterations ended up with 0265-PRN21, 0392-PRN26, 0348-PRN21, and 0689-PRN26 geometries. The LOS of PRN21 from 0265 station was found to intersect with the acoustic waves, generated by the Rayleigh wave source RW640.78, at atmospheric altitude of 198 km. The CIP detection altitude for 0392-PRN26 geometry was estimated as 159 km for source RW634.34. The uncertainty in locating the suitable ground sources was ±3.22 km, which is well within the tolerable error as described earlier. The CIP detection altitudes for 0348-PRN21 and 0689-PRN26 geometries have been estimated as 202 and 176 km, respectively. The respective responsible sources were found to be RW972.44 and RW969.22. The outcome of the analysis is presented in Table 1 for ready reference. In addition, the elevation angle of the satellites used in the present study along with the corresponding detection altitudes is shown in Figure S3 in Supporting Information S1. From Table 1, it can be seen that, despite low elevation angle (∼25°) of PRN26 from station 0689, the estimated detection altitude is relatively higher as compared to 0392-PRN26 and 0260-PRN26 geometries. This might be due to the considered seismic source distribution. The sources are assumed based on the average Rayleigh wave velocity, which do not consider the velocity variations arising from the different geological terrains. Further, the model-derived atmospheric parameters used in the seismo-acoustic ray tracing can also contribute to this. Detailed study with different approaches may be taken up in future to resolve this.

5. Conclusion

Estimation of actual detection altitudes of Rayleigh wave generated ionospheric perturbations observed in GPS-TEC has been attempted during the Tohoku-Oki earthquake. The average Rayleigh wave velocity over the Japan region was estimated using the seismic waveform data recorded during the event. Using the 3D ray tracing of Rayleigh wave generated acoustic waves in the atmosphere and realistic GPS station-satellite LOS geometry, our analysis not only computed the detection altitudes of ionospheric perturbations measured in GPS-TEC but also demonstrated the possibility of detecting specific CIP at different ionospheric altitudes, based on the distinct satellite geometries.

Data Availability Statement

GEONET 1-Hz GPS data can be obtained from the Geospatial Information Authority of Japan (www.gsi.go.jp). Seismic wave form data can be obtained from the National Research Institute for Earth Science and Disaster Resilience (NIED)-F-net (www.fnet.bosai.go.jp).

References

Artru, J., Ducic, V., Kanamori, H., Lognonne, P., & Murakami, M. (2005). Ionospheric detection of gravity waves induced by tsunamis. *Geophysical Journal International*, *160*(3), 840–848. https://doi.org/10.1111/j.1365-246x.2005.02552.x

Artru, J., Farges, T., & Lognonn, P. (2004). Acoustic waves generated from seismic surface waves: Propagation properties determined from Doppler sounding observations and normal-mode modelling. *Geophysical Journal International*, *158*, 1067–1077. https://doi.org/10.1111/j.1365-246X.2004.02377.x

Astafyeva, E., Heki, K., Kiryushkin, V., Afraimovich, E., & Shalimov, S. (2009). Two-mode long-distance propagation of coseismic ionosphere disturbances. *Journal of Geophysical Research*, *114*, A10307. https://doi.org/10.1029/2008JA013853

Astafyeva, E., Lognonné, P., & Rolland, L. (2011). First ionospheric images of the seismic fault slip on the example of the Tohoku-Oki earthquake. *Geophysical Research Letters*, *38*, L22104. https://doi.org/10.1029/2011GL049623

Astafyeva, E., Rolland, L., Lognonné, P., Khelfi, K., & Yahagi, T. (2013). Parameters of seismic source as deduced from 1 Hz ionospheric GPS data: Case study of the 2011 Tohoku-Oki event. *Journal of Geophysical Research: Space Physics*, *118*, 5942–5950. https://doi.org/10.1002/jgra.50556

Astafyeva, E., & Shults, K. (2019). Ionospheric GNSS imagery of seismic source: Possibilities, difficulties, and challenges. *Journal of Geophysical Research: Space Physics*, *124*, 534–543. https://doi.org/10.1029/2018JA026107

Bagiya, M. S., Sunil, A. S., Sunil, P. S., Sreejith, K. M., Rolland, L., & Ramesh, D. S. (2017). Efficiency of coseismic ionospheric perturbations in identifying crustal deformation pattern: Case study based on Mw 7.3 May Nepal 2015 earthquake. *Journal of Geophysical Research: Space Physics*, *122*, 6849–6857. https://doi.org/10.1002/2017JA024050

Bagiya, M. S., Thomas, D., Astafyeva, E., Bletery, Q., Lognonné, P., & Ramesh, D. S. (2020). The ionospheric view of the 2011 Tohoku-Oki earthquake seismic source: The first 60 seconds of the rupture. *Scientific Reports*, *10*, 5232. https://doi.org/10.1038/s41598-020-61749-x

Bilitza, D., Altadill, D., Truhlik, V., Shubin, V., Galkin, I., Reinisch, B., & Huang, X. (2017). International Reference Ionosphere 2016: From ionosphere climate to real-time weather predictions. *Space Weather*, *15*, 418–429. https://doi.org/10.1002/2016SW001593

Calais, E., & Minster, J. B. (1995). GPS detection of ionospheric perturbations following the January 17, 1994, Northridge earthquake. *Geophysical Research Letters*, *22*(9), 1045–1048.

Coisson, P., Lognonne, P., Walwer, D., & Rolland, L. M. (2015). First tsunami gravity wave detection in ionospheric radio occultation data. *Earth and Space Science*, *2*, 125–133. https://doi.org/10.1002/2014EA000054

Davies, K., & Baker, D. M. (1965). Ionospheric effects observed around the time of the Alaskan earthquake. *Journal of Geophysical Research*, *70*(9), 2251–2253.

Ducic, V., Artru, J., & Lognonne, P. (2003). Ionospheric remote sensing of the Denali Earthquake Rayleigh surface waves. *Geophysical Research Letters*, *30*(18), 1951. https://doi.org/10.1029/2003GL017812

Havskov, J., & Ottemöller, L. (1999). SEISAN earthquake analysis software. *Seismological Research Letters*, *70*(5), 532–534. https://doi.org/10.1785/gssrl.70.5.532

Heki, K., & Ping, J. (2005). Directivity and apparent velocity of the coseismic ionospheric disturbances observed with a dense GPS array. *Earth and Planetary Science Letters*, *236*, 845–855. https://doi.org/10.1016/j.epsl.2005.06.010

Jin, S., Jin, R., & Li, J. H. (2014). Pattern and evolution of seismo-ionospheric disturbances following the 2011 Tohoku earthquakes from GPS observations. *Journal of Geophysical Research: Space Physics*, *119*, 7914–7927. https://doi.org/10.1002/2014JA019825

Jin, S., Occhipinti, G., & Jin, R. (2015). GNSS ionospheric seismology: Recent observation evidences and characteristics. *Earth-Science Reviews*, *147*, 54–64.

Kakinami, Y., Yamamoto, M., Chen, C. H., Watanabe, S., Lin, C., Liu, J. Y., & Habu, H. (2013). Ionospheric disturbances induced by a missile launched from North Korea on 12 December 2012. *Journal of Geophysical Research: Space Physics*, *118*, 5184–5189. https://doi.org/10.1002/jgra.50508

Komjathy, A., Yang, Y.-M., Meng, X., Verkhoglyadova, O., Mannucci, A. J., & Langley, R. B. (2016). Review and perspectives: Understanding natural-hazards-generated ionospheric perturbations using GPS measurements and coupled modeling. *Radio Science*, *51*, 951–961. https://doi.org/10.1002/2015RS005910

Leonard, R. S., & Barnes, R., Jr. (1965). Observation of ionospheric disturbances following the Alaska earthquake. *Journal of Geophysical Research*, *70*(5), 1250–1253.

Liu, J. Y., Chen, C. H., Lin, C. H., Tsai, H. F., Chen, C. H., & Kamogawa, M. (2011). Ionospheric disturbances triggered by the 11 March 2011 M9.0 Tohoku earthquake. *Journal of Geophysical Research*, *116*, A06319. https://doi.org/10.1029/2011JA016761

Liu, J. Y., Chen, C. H., Sun, Y. Y., Chen, C. H., Tsai, H. F., Yen, H. Y., et al. (2016). The vertical propagation of disturbances triggered by seismic waves of the 11 March 2011 M9.0 Tohoku earthquake over Taiwan. *Geophysical Research Letters*, *43*, 1759–1765. https://doi.org/10.1002/2015GL067487

Liu, J.-Y., Tsai, Y.-B., Ma, K.-F., Chen, Y.-I., Tsai, H.-F., Lin, C.-H., et al. (2006). Ionospheric GPS total electron content (TEC) disturbances triggered by the 26 December 2004 Indian ocean tsunami. *Journal of Geophysical Research*, *111*, A05303. https://doi.org/10.1029/2005JA011200

Liu, Y., & Jin, S. (2019). Ionospheric Rayleigh wave disturbances following the 2018 Alaska earthquake from GPS observations. *Remote Sensing*, *11*(8), 901.

Lognonné, P., Karakostas, F., Rolland, L., & Nishikawa, Y. (2016). Modeling of atmospheric-coupled Rayleigh waves on planets with atmosphere: From Earth observation to Mars and Venus perspectives. *Journal of the Acoustical Society of America*, *140*(2), 1447–1468.

Makela, J. J., Lognonne, P., Hébert, H., Gehrels, T., Rolland, L., Allgeyer, S., et al. (2011). Imaging and modeling the ionospheric airglow response over Hawaii to the tsunami generated by the Tohoku earthquake of 11 March 2011. *Geophysical Research Letters*, *38*, L00G02. https://doi.org/10.1029/2011GL047860

Maruyama, T., Shinagawa, H., Yusupov, K., & Akchurin, A. (2017). Sensitivity of ionosonde detection of atmospheric disturbances induced by seismic Rayleigh waves at different latitudes. *Earth Planets and Space*, *69*(1), 20. https://doi.org/10.1186/s40623-017-0600-z

Najita, K., & Yuen, P. (1979). Long-period oceanic Rayleigh wave group velocity dispersion curve from HF Doppler sounding of the ionosphere. *Journal of Geophysical Research*, *84*(A4), 1253–1260.

Occhipinti, G., Aden-Antoniow, F., Bablet, A., Molinie, J.-P., & Farges, T. (2018). Surface waves magnitude estimation from ionospheric signature of Rayleigh waves measured by Doppler sounder and OTH radar. *Scientific Reports*, *8*(1), 1555. https://doi.org/10.1038/s41598-018-19305-1

Occhipinti, G., Dorey, P., Farges, T., & Lognonn, P. (2010). Nostradamus: The radar that wanted to be a seismometer. *Geophysical Research Letters*, *37*, L18104. https://doi.org/10.1029/2010GL044009

Occhipinti, G., Rolland, L., Lognonne, P., & Watada, S. (2013). From Sumatra 2004 to Tohoku-Oki 2011: The systematic GPS detection of the ionospheric signature induced by tsunamigenic earthquakes. *Journal of Geophysical Research: Space Physics*, *118*, 3626–3636. https://doi.org/10.1002/jgra.50322

Otsuka, Y., Kotake, N., Tsugawa, T., Shiokawa, K., Ogawa, T., Saito, S., et al. (2006). GPS detection of total electron content variations over Indonesia and Thailand following the 26 December 2004 earthquake. *Earth Planets and Space*, *58*(2), 159–165.

Ozeki, M., & Heki, K. (2010). Ionospheric holes made by ballistic missiles from North Korea detected with a Japanese dense GPS array. *Journal of Geophysical Research*, *115*, A09314. https://doi.org/10.1029/2010JA015531

Rolland, L. M., Lognonné, P., & Munekane, H. (2011). Detection and modeling of Rayleigh wave induced patterns in the ionosphere. *Journal of Geophysical Research*, *116*, A05320. https://doi.org/10.1029/2010JA016060

Sunil, A. S., Bagiya, M. S., Catherine, J., Rolland, L., Sharma, N., Sunil, P. S., & Ramesh, D. S. (2017). Dependence of near field co-seismic ionospheric perturbations on surface deformations: A case study based on the April, 25 2015 Gorkha Nepal earthquake. *Advances in Space Research*, *59*(5), 12001208. https://doi.org/10.1016/j.asr.2016.11.041

Sunil, A. S., Bagiya, M. S., Reddy, C. D., Kumar, M., & Ramesh, D. S. (2015). Post-seismic ionospheric response to the 11 April 2012 East Indian Ocean doublet earthquake. *Earth Planets and Space*, *67*(1), 37. https://doi.org/10.1186/s40623-015-0200-8

Takagi, N., Sato, H., Nishimura, T., & Obara, K. (2006). *Rayleigh-wave group velocity in Japan revealed from the cross-correlation analysis of microseisms excited by typhoons*. In *Proceedings of the 8th SEGJ International Symposium* (Vol. 1–4). Society of Exploration Geophysicists of Japan.

Thomas, D., Bagiya, M. S., Sunil, P. S., Rolland, L., Sunil, A. S., Mikesell, T. D., & Nayak, S. (2018). Revelation of early detection of co-seismic ionospheric perturbations in GPS-TEC from realistic modelling approach: Case study. *Scientific Reports*, *8*(1), 12105. https://doi.org/10.1038/s41598-018-30476-9

Tsugawa, T., Saito, A., Otsuka, Y., Nishioka, M., Maruyama, T., Kato, H., et al. (2011). Ionospheric disturbances detected by GPS total electron content observation after the 2011 off the Pacific coast of Tohoku Earthquake. *Earth Planets and Space*, *63*(7), 875–879.

Weaver, P. F., Yuen, P. C., & Prolss, G. W. (1970). Acoustic coupling into the ionosphere from seismic waves of the earthquake at Kurile Islands on August 11, 1969. *Nature*, *226*, 1239–1241. https://doi.org/10.1038/2261239a0

Witek, M., Van Der Lee, S., & Kang, T. S. (2014). Rayleigh wave group velocity distributions for East Asia using ambient seismic noise. *Geophysical Research Letters*, *41*, 8045–8052. https://doi.org/10.1002/2014GL062016

Yuen, P. C., Weaver, P. F., Suzuki, R. K., & Furumoto, A. S. (1969). Continuous, traveling coupling between seismic waves and the ionosphere evident in May 1968 Japan earthquake data. *Journal of Geophysical Research*, *74*(9), 2256–2264.

Zumberge, J., Heflin, M., Jefferson, D., Watkins, M., & Webb, F. (1997). Precise point positioning for the efficient and robust analysis of GPS data from large networks. *Journal of Geophysical Research*, *102*(B3), 5005–5017.